A

B

Fig. 2. Diiron structure of TAO. (A) Stereo view of the diiron active site and its environment. Diiron and hydroxo atoms are shown as magenta spheres, four glutamate and two histidine residues important for diiron binding as green sticks, neighboring residues within 6 Å of the diiron in yellow, nitrogen in blue, and oxygen in red. (B) Stereo view of the coordinate bonds (solid lines) and hydrogen bonds (dashed lines) of the diiron active site. Sigma-A weighted electron density map calculated from the refined model of the ligand-free TAO with the diiron centers omitted from the phase calculation is also shown. Contour levels are 1.0 σ (blue) and 3.0 σ (orange). H165 forms hydrogen bonds with E123, E162, and N161 and H269 with E162, E213, and N161. N161, which is situated in the center of the hydrogen network, forms additional hydrogen bonds with Y246 and D265. D265 forms hydrogen bonds with W65 and W247.

an oxidized diiron active site that is ligated solely by carboxylate ligands. In contrast, diiron active sites of soluble diiron proteins with known structures, Δ^4 ACP desaturase (27) (PDB ID code 2UW1), methane monooxygenase (28) (PDB ID code 1MMO), rubrerythrin (29) (PDB ID code 1LKM), and ribonucleotide reductase R2 subunit (30) (PDB ID code 1RIB), are all coordinated by at least one if not two histidine residues.

Important Tyrosine Residues. Similar to ribonucleotide reductase, tyrosine residues have also been proposed to play an essential role in the catalytic cycle of AOX (1, 31, 32). Scrutiny of *SI Appendix*, Fig. S5 reveals that although there seem to be four conserved tyrosine residues (Y198, Y211, Y220, and Y246), only three of which (not Y211) are totally conserved across all amino acid sequences of membrane-bound AOXs, including the plastid AOX (33). Y220 is buried deep within the four-helix bundle and within 4 Å of the diiron center (Fig. 2A), making it the most likely candidate for the amino acid radical involved in the catalytic cycle (32). Indeed, Y220 is absolutely conserved across all AOXs sequenced to date, and mutational analyses have unequivocally demonstrated that this residue is critical for enzymatic activity of all AOXs (1, 33). Y198 has been proposed to be involved in ubiquinol binding, although its mutation does

not lead to the complete loss of activity (18, 34). The crystal structure of TAO (*SI Appendix*, Fig. S7) indicates that Y198, located on the C-terminal portion of helix α4, is separated by more than 15 Å from the diiron center and forms a hydrogen bond with a conserved H206 protruding from the N-terminal portion of helix α5. Such a position suggests it probably stabilizes the structure of TAO rather than being directly involved in ubiquinol binding. Although Y246 on helix S3 is located 10.7 ± 0.2 Å from the diiron center, which is within electron tunneling distance [<14 Å (35)], it is more likely to be involved in the hydrogen-bonding network rather than electron transport, because it is 2.9 ± 0.2 Å from N161 in helix α3 (Fig. 2B and *SI Appendix*, Fig. S7). This notion is supported by the result that a Y246A mutant retains some activity (1, 34), which would not be the case if it were essential for electron transfer.

Binding Mode of the Potent Inhibitor AF2779OH. Until recently little structural information was available on the mode of AF binding to TAO, even given its specificity. Inhibitor kinetic studies indicated that AF showed a mixed-type inhibition against ubiquinol (23), suggesting that the ring moiety and the geranyl portions of AF are important for the interaction of the inhibitor with TAO. To investigate whether this was the case, an AF derivative lacking the furanone ring was synthesized (AF2779OH: 5-chloro-3-[(2E,6E)-8-hydroxy-3,7-dimethylnona-2,6-dienyl]-2,4-dihydroxy-6-methylbenzaldehyde; Fig. 3A). AF2779OH possesses similar inhibitory properties (IC$_{50}$ = 0.48 nM for TAO; minimum inhibitory concentration = 30 nM for *T. brucei brucei*) to AF, indicating that the furanone ring is indeed not critical for inhibitory activity, thereby rendering it useful to determine the location of AF binding to TAO. A crystal of the TAO–AF2779OH complex was prepared by soaking in the cryoprotectant solution supplemented with the inhibitor and the structure determined at 2.6 Å by molecular replacement using the inhibitor-free TAO structure as a template (*SI Appendix*, Table S1 and Fig. S1B). In addition, the crystal structure of TAO complexed with CCB, another AF derivative (5-chloro-3-[(2E)-3,7-dimethylocta-2,6-dienyl]-2,4-dihydroxy-6-methylbenzaldehyde), was also determined at 2.3 Å resolution (*SI Appendix*, Table S1 and Fig. S1C). *SI Appendix*, Figs. S8 and S9 show that CCB is bound to the enzyme in a manner similar to AF2779OH. CCB also strongly inhibits TAO (IC$_{50}$ = 0.20 nM for TAO); however, unlike AF and AF2779OH, it is toxic to mice. Given the toxicity of CCB we will therefore focus further discussion on the structure of TAO complexed with AF2779OH, because it is a safer drug candidate for trypanosomiasis.

Fig. 3 B and C show the dimeric structure of the TAO–AF2779OH complex and residues around the bound AF2779OH, respectively. The binding cavity of AF2779OH is located near the membrane surface between helices α1 and α4 and is lined by 16 highly conserved residues (V92, R96, F99, R118, C119, F121, L122, E123, V125, M190, L212, E213, E215, A216, T219, and Y220) plus C95 (Fig. 3C and *SI Appendix*, Figs. S5 and S8 and Table S3). It is also apparent from Fig. 3C and *SI Appendix*, Fig. S8 and Table S3 that the aromatic head of AF2779OH is located close to the diiron active site and the C2–OH forms hydrogen bonds with R118 and T219. In addition, the aldehyde oxygen at the C1 position interacts with E123 through a hydrogen bond network, C1–CH = O···C119–SH···Y220–OH···E123–COO⁻, in the B and D subunit, whereas the aldehyde oxygens of the A and C subunits form an intrasubunit hydrogen bond with C2–OH. These hydrogen bonds are also observed in the TAO–CCB complex and seem to be important for the potent inhibitory activities of both inhibitors. Indeed, IC$_{50}$ values of AF derivatives lacking this aldehyde group (K2-9 and K4-9 in *SI Appendix*, Fig. S10) increase substantially (36). It is also likely that van der Waals contacts formed between AF2779OH and TAO (*SI Appendix*, Table S3) contribute to the potent effect of these inhibitors (36). In the inhibited enzymes the distances between H165 and Fe1 (2.3 ± 0.1 and 2.4 ± 0.1 Å for AF2779OH and CCB, respectively) are shorter than that observed in the inhibitor-free structure (3.5 ± 0.3 Å), and hence H165 can now
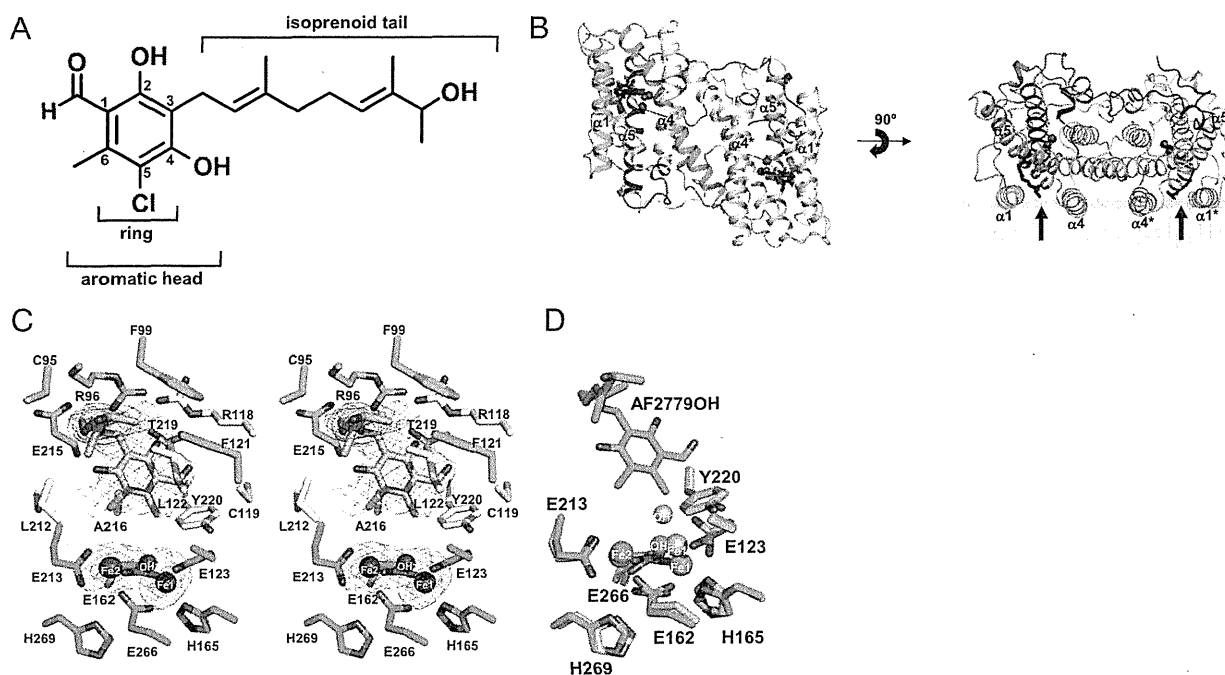
Fig. 3. Structure of the TAO–AF2779OH complex. (*A*) The chemical structure of AF2779OH. (*B*) Overall structure of the TAO–AF2779OH complex. AF2779OH is shown as a red stick. Chains A and B are shown as rainbow (colored blue to red from N to C terminus) and gray, respectively. The AF2779OH-binding cavity is shown by an arrow. (*C*) Stereo view of the AF2779OH binding region of chain A. The residues that interact with AF2779OH (pink stick) -ring and -tail are shown as yellow and cyan sticks, respectively. N, O, and Cl atoms are colored in blue, red, and green, respectively. Sigma-A weighted electron density map calculated from the refined model of the TAO–AF2779OH complex with the diiron centers and AF2779OH molecules omitted from the phase calculation is also shown. Contour levels are 1.0 σ (blue) and 3.0 σ (orange). (*D*) Superimposed diiron active sites of AF2779OH-free (light pink) and -bound (green) forms of TAO. The binding of AF2779OH causes the formation of a coordinate bond between H165 and Fe1.

coordinate with Fe1, unlike H269, which is still separated by 4.3 ± 0.2 Å from Fe2 in both cases (Fig. 3*D* and *SI Appendix*, Fig. S12 and Table S2).

Mutational Analysis of Functionally Relevant Residues. *SI Appendix*, Table S4 summarizes the catalytic activities of the mutated recombinant proteins that were measured in isolated membrane fractions from each *Escherichia coli* culture. It is apparent from *SI Appendix*, Table S4 that all mutated residues that interact either with the diiron (E213A) or the inhibitor (R118A, R118Q, L122A, L122N, E215A, A216L, A216N, T219V, and Y220F; Fig. 4) resulted in almost complete loss of ubiquinol oxidizing activity. Furthermore, the Y246A mutant, which participates in the hydrogen bond network (Fig. 2), also resulted in significant inhibition of catalytic activity. We believe that these residues are important for the correct conformation of the diiron center and interaction with AF2779OH and are consistent with the crystal structure.

Ubiquinol Binding Model. In addition to the inhibitor-binding cavity observed in Figs. 3*B* and 5 *A* and *C*, which is comparable to that observed in other monotopic proteins such as prostaglandin H$_2$ synthase (37), CAVER protein-analysis software (38) predicts that there is another possible hydrophobic cavity near the membrane surface (Fig. 5 *A* and *D*). This second cavity connects the diiron active site with the membrane exterior and interacts with the inhibitor-binding cavity at the active site. It is formed by residues from helices α1 (R96 and D100), α2 (R118, L122, E123, and A126), α3 (E162 and H165), α5 (L212, E213, E215, A216, and T219), and α6 (E266), which, similar to that observed in the inhibitor-binding cavity, are also highly conserved (*SI Appendix*, Fig. S5). It is apparent from Fig. 5 *A* and *D* that a part of the aromatic head group of AF2779OH enters this second cavity. Based on the structure of the TAO–AF2779OH complex, a ubiquinol-binding model was built by superposing

a ubiquinol molecule onto the bound AF2779OH. The model (Fig. 5*B*) indicates that the distance between ubiquinol C4–OH and Fe2 is 4.3 Å and C1–OH is connected to the outside of TAO through a hydrogen bond network, C1–OH···R118···D100 (Fig. 5*B*). On the basis of the structures reported in this study we propose that each hydrophobic cavity binds one ubiquinol close to the active site with their quinol rings located at the bottom of each cavity in a manner similar to AF2779OH. Although the exact route of electron transfer for the four-electron reduction of oxygen to water in any alternative oxidase is unresolved at the present time, we suggest the process involves both ubiquinols and Tyr220
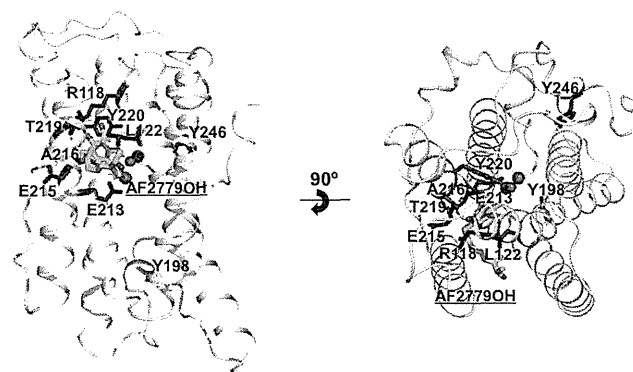

Fig. 4. Location of the recombinant TAO mutations within the protein. Diiron and hydroxo atoms are shown as magenta spheres. AF2779OH is shown as a cyan stick. Red sticks show the mutated residues that almost completely abolished activity (specific activity <10%), whereas yellow sticks show the mutated residues that retained some residual activity (specific activity ≥10%).

– 481 –

(39). During the sequential electron reduction process we suggest that following the activation of oxygen, free radicals are generated on a tightly bound ubiquinol and Tyr220. The ubisemiquinol is then reoxidized by the tyrosine radical generated during the catalytic cycle and the reduction process is completed following full oxidation of a loosely bound ubiquinol (39).

Conclusions

The TAO structures reported in this study are a high-resolution view of a membrane bound diiron-carboxylate protein. Although the crystal structures support earlier modeling studies (13, 14, 22) that suggested that the alternative oxidases are monotopic proteins in which the diiron active site is coordinated by carboxylate and histidine residues, they did reveal that in the oxidized state only carboxylate residues act as the coordinating ligands. Such a primary ligation sphere, although unusual for diiron proteins in the oxidized state, is, however, consistent with our earlier reduced minus oxidized IR difference spectra (26). This study clearly demonstrated that upon reduction of purified TAO there was a net protonation of at least one carboxylate residue in addition to alterations in the signals associated with histidine residues consistent with the notion that the oxidation–reduction cycle of the alternative oxidases involves major conformational perturbations and carboxylate shifts. The structure has also revealed that the redox-active Y220, which is totally conserved across all AOXs (1), is within 4 Å of the active site. Such a close-range electron transfer position, comparable to that observed in the R2 subunit of ribonucleotide reductase (31), is further support for the suggestion that radicals play a key role in the AOX catalytic cycle (39).

In addition to providing a structural insight into the active site of this enigmatic protein our structures have also revealed the nature of the inhibitor binding site. The binding site of our AF derivative was within 4 Å of not only the diiron center but also Y220 and resulted in some dramatic conformational changes such that H165 moved within ligating distance of Fe (1). CAVER protein analysis software (38) suggested that the inhibitor-binding cavity connects at the diiron center with an additional cavity, which could also serve as a ubiquinone binding site.

In conclusion, we believe that the structures presented in this report will contribute to a more complete understanding of the function and inhibition of all AOXs. It will not only be beneficial for the control of trypanosomiasis and other human diseases, such as cryptosporidiosis and candidiasis, but also for the control of plant diseases caused by phytopathogenic fungi (1, 40).

Materials and Methods

Crystallization. The oxidized form of alternative oxidase from *Trypanosoma brucei brucei* was expressed, purified, and crystallized essentially according to the method described previously (23, 24) using 28–34% (wt/vol) PEG 400, 100 mM imidazole buffer (pH 7.4), and 500 mM potassium formate as the reservoir solution. Detailed information is presented in *SI Appendix, SI Materials and Methods*.

Data Collection and Phasing. For phasing by the single-wavelength anomalous dispersion (SAD) method, anomalous scattering effects caused by Fe were measured to 3.2 Å resolution. The dataset was processed and scaled with HKL2000 (41). The program SOLVE (42) was used to locate and refine four "diiron sites" (figure of merit = 0.195). The RESOLVE (43) program was used for solvent flattening (figure of merit = 0.645). The resulting electron density map was clear enough to trace the TAO molecules. Initial models were built
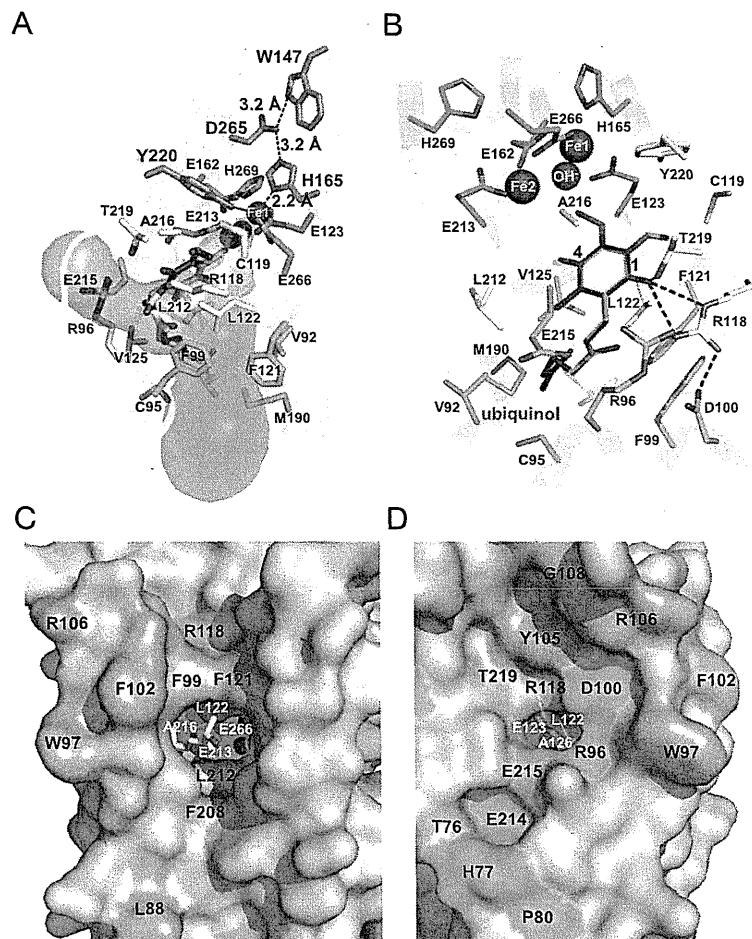
Fig. 5. Putative ubiquinol binding cavities in TAO. (*A*) Two hydrophobic cavities predicted by CAVER protein-analysis software (38). The bound AF2779OH (isoprenoid tail) occupies the green cavity. Putative residues involved in electron transfer are shown as orange sticks. (*B*) Ubiquinol binding model predicted by the superposition of a ubiquinol molecule (purple stick) onto the bound AF2779OH (translucent white stick) of the TAO–AF2779OH complex. Magenta spheres are diiron (Fe–OH⁻–Fe), the green stick represents residues coordinating to diiron, and yellow and cyan sticks are residues interacting with the aromatic head and isoprenoid tail, respectively. Hydrogen bonds are depicted as dotted lines. Surface views of the (*C*) green and (*D*) orange cavities shown in *A*. Cyan and pink colors stand for conservation of AOX residues in all eight and over four organisms in *SI Appendix*, Fig S5, respectively.

using RESOLVE (43) and BUCANER (43). Detailed analysis of diffraction data showed that the crystal used for the data collection of Fe-SAD was pseudohemihedral twinning. Amplitude-based twin-refinement using REFMAC5 (45) decreased R_{work}/R_{free} drastically from 0.307/0.363 to 0.250/0.310. X-ray diffraction data of ligand-free TAO and AF derivatives complex crystals were collected to 2.85, 2.6, and 2.3 Å resolution, respectively. All datasets were processed and scaled with HKL2000 (42). Detail information is presented in *SI Appendix, SI Materials and Methods*.

Refinement. The initial model of inhibitor-free TAO was determined by molecular replacement (MR) using the model obtained by SAD (3.2 Å resolution) as a search model. The program Phaser (46) in CCP4i was used for MR. The models of ligand-free TAO and TAO-AF2779OH complex were rebuilt with reference to the well-refined model of the TAO–CCB complex at 2.3 Å resolution. Manual rebuilding and crystallographic refinement of all structures were performed using COOT (47) and REFMAC5 (45). All structures were refined by amplitude-based twin-refinement in REFMAC5 (45) to final R_{work}/R_{free} values of 0.192/0.247 (twin fraction of 0.476), 0.214/0.256 (twin fraction of 0.552), and 0.185/0.227 (twin fraction of 0.527) for ligand-free TAO, TAO–AF2779OH, and TAO–CCB, respectively. The omit electron density maps of ligand-free TAO, TAO–AF2779OH, and TAO–CCB around helix 5 are shown in *SI Appendix*, Fig. S14. On average, about 30 residues of N and C termini of TAO were missing as a result of flexibility. Data collection and structural refinement statistics are summarized in *SI Appendix*, Table S1. Figures showing protein structures were prepared with the graphics program PyMol (www.pymol.org). Detailed information is presented in *SI Appendix, SI Materials and Methods*.

1. Moore AL, Albury MS (2008) Further insights into the structure of the alternative oxidase: From plants to parasites. *Biochem Soc Trans* 36(Pt 5):1022–1026.
2. McDonald AE, Vanlerberghe GC (2006) Origins, evolutionary history, and taxonomic distribution of alternative oxidase and plastoquinol terminal oxidase. *Comp Biochem Physiol Part D Genomics Proteomics* 1(3):357–364.
3. Chaudhuri M, Ajayi W, Hill GC (1998) Biochemical and molecular properties of the *Trypanosoma brucei* alternative oxidase. *Mol Biochem Parasitol* 95(1):53–68.
4. Roberts CW, et al. (2004) Evidence for mitochondrial-derived alternative oxidase in the apicomplexan parasite *Cryptosporidium parvum*: A potential anti-microbial agent target. *Int J Parasitol* 34(3):297–308.
5. Chaudhuri M, Ott RD, Hill GC (2006) Trypanosome alternative oxidase: From molecule to function. *Trends Parasitol* 22(10):484–491.
6. Phillips MA (2012) Stoking the drug target pipeline for human African trypanosomiasis. *Mol Microbiol* 86(1):10–14.
7. Zíkova A, Schnaufer A, Dalley RA, Panigrahi AK, Stuart KD (2009) The Fo-F1-ATP synthase complex contains novel subunits and is essential for procyclic *Trypanosoma brucei*. *PLoS Pathog* 5:1–15.
8. Opperdoes FR, Borst P, Bakker S, Leene W (1977) Localization of glycerol-3-phosphate oxidase in the mitochondrion and particulate NAD+-linked glycerol-3-phosphate dehydrogenase in the microbodies of the bloodstream form to *Trypanosoma brucei*. *Eur J Biochem* 76(1):29–39.
9. Nihei C, Fukai Y, Kita K (2002) Trypanosome alternative oxidase as a target of chemotherapy. *Biochim Biophys Acta* 1587(2–3):234–239.
10. Minagawa N, et al. (1997) An antibiotic, ascofuranone, specifically inhibits respiration and in vitro growth of long slender bloodstream forms of *Trypanosoma brucei brucei*. *Mol Biochem Parasitol* 84(2):271–280.
11. Yabu Y, et al. (2003) The efficacy of ascofuranone in a consecutive treatment on *Trypanosoma brucei brucei* in mice. *Parasitol Int* 52(2):155–164.
12. Yabu Y, et al. (2006) Chemotherapeutic efficacy of ascofuranone in *Trypanosoma vivax*-infected mice without glycerol. *Parasitol Int* 55(1):39–43.
13. Andersson ME, Nordlund P (1999) A revised model of the active site of alternative oxidase. *FEBS Lett* 449(1):17–22.
14. Berthold DA, Andersson ME, Nordlund P (2000) New insight into the structure and function of the alternative oxidase. *Biochim Biophys Acta* 1460(2-3):241–254.
15. Albury MS, Affourtit C, Moore AL (1998) A highly conserved glutamate residue (Glu-270) is essential for plant alternative oxidase activity. *J Biol Chem* 273(46):30301–30305.
16. Ajayi WU, Chaudhuri M, Hill GC (2002) Site-directed mutagenesis reveals the essentiality of the conserved residues in the putative diiron active site of the trypanosome alternative oxidase. *J Biol Chem* 277(10):8187–8193.
17. Albury MS, Affourtit C, Crichton PG, Moore AL (2002) Structure of the plant alternative oxidase. Site-directed mutagenesis provides new information on the active site and membrane topology. *J Biol Chem* 277(2):1190–1194.
18. Nakamura K, et al. (2005) Mutational analysis of the *Trypanosoma vivax* alternative oxidase: The E(X)$_6$Y motif is conserved in both mitochondrial alternative oxidase and plastid terminal oxidase and is indispensable for enzyme activity. *Biochem Biophys Res Commun* 334(2):593–600.
19. Berthold DA, Voevodskaya N, Stenmark P, Gräslund A, Nordlund P (2002) EPR studies of the mitochondrial alternative oxidase. Evidence for a diiron carboxylate center. *J Biol Chem* 277(46):43608–43614.
20. Moore AL, et al. (2008) Compelling EPR evidence that the alternative oxidase is a diiron carboxylate protein. *Biochim Biophys Acta* 1777(4):327–330.
21. Nordlund P, Eklund H (1995) Di-iron-carboxylate proteins. *Curr Opin Struct Biol* 5(6):758–766.
22. Berthold DA, Stenmark P (2003) Membrane-bound diiron carboxylate proteins. *Annu Rev Plant Biol* 54:497–517.
23. Kido Y, et al. (2010) Purification and kinetic characterization of recombinant alternative oxidase from *Trypanosoma brucei brucei*. *Biochim Biophys Acta* 1797(4):443–450.
24. Kido Y, et al. (2010) Crystallization and preliminary crystallographic analysis of cyanide-insensitive alternative oxidase from *Trypanosoma brucei brucei*. *Acta Crystallogr Sect F Struct Biol Cryst Commun* 66(Pt 3):275–278.
25. Lomize MA, Pogozheva ID, Joo H, Mosberg HI, Lomize AL (2012) OPM database and PPM web server: Resources for positioning of proteins in membranes. *Nucleic Acids Res* 40(Database issue):D370–D376.
26. Maréchal A, Kido Y, Kita K, Moore AL, Rich PR (2009) Three redox states of *Trypanosoma brucei* alternative oxidase identified by infrared spectroscopy and electrochemistry. *J Biol Chem* 284(46):31827–31833.
27. Guy JE, Whittle E, Kumaran D, Lindqvist Y, Shanklin J (2007) The crystal structure of the ivy Δ^4-16:0-ACP desaturase reveals structural details of the oxidized active site and potential determinants of regioselectivity. *J Biol Chem* 282(27):19863–19871.
28. Rosenzweig AC, Frederick CA, Lippard SJ, Nordlund P (1993) Crystal structure of a bacterial non-haem iron hydroxylase that catalyses the biological oxidation of methane. *Nature* 366(6455):537–543.
29. Jin S, Kurtz DM, Jr., Liu ZJ, Rose J, Wang BC (2002) X-ray crystal structures of reduced rubrerythrin and its azide adduct: A structure-based mechanism for a non-heme diiron peroxidase. *J Am Chem Soc* 124(33):9845–9855.
30. Nordlund P, Eklund H (1993) Structure and function of the *Escherichia coli* ribonucleotide reductase protein R2. *J Mol Biol* 232(1):123–164.
31. Schmidt PP, Rova U, Katterle B, Thelander L, Gräslund A (1998) Kinetic evidence that a radical transfer pathway in protein R2 of mouse ribonucleotide reductase is involved in generation of the tyrosyl free radical. *J Biol Chem* 273(34):21463–21472.
32. Affourtit C, Albury MS, Crichton PG, Moore AL (2002) Exploring the molecular nature of alternative oxidase regulation and catalysis. *FEBS Lett* 510(3):121–126.
33. McDonald AE (2009) Alternative oxidase: What information can protein sequence comparisons give us? *Physiol Plant* 137(4):328–341.
34. Albury MS, Elliott C, Moore AL (2010) Ubiquinol-binding site in the alternative oxidase: Mutagenesis reveals features important for substrate binding and inhibition. *Biochim Biophys Acta* 1797(12):1933–1939.
35. Page CC, Moser CC, Chen X, Dutton PL (1999) Natural engineering principles of electron tunnelling in biological oxidation-reduction. *Nature* 402(6757):47–52.
36. Saimoto H, Kido Y, Haga Y, Sakamoto K, Kita K (2013) Pharmacophore identification of ascofuranone, potent inhibitor of cyanide-insensitive alternative oxidase of Trypanosoma brucei. *J Biochem* 153(3):267–273.
37. Picot D, Loll PJ, Garavito RM (1994) The X-ray crystal structure of the membrane protein prostaglandin H$_2$ synthase-1. *Nature* 367(6460):243–249.
38. Medek P, Benes P, Sochor J (2007) Computation of tunnels in protein molecules using Delaunay triangulation. *J WSCG* 15:107–114.
39. Moore AL, et al. (2013) Unraveling the heater – New insights into the structure of the alternative. *Annu Rev Plant Biol*, in press.
40. Fernández-Ortuño D, Torés JA, de Vicente A, Pérez-García A (2008) Mechanisms of resistance to QoI fungicides in phytopathogenic fungi. *Int Microbiol* 11(1):1–9.
41. Otwinowski Z, Minor W (1997) Processing of X-ray diffraction data collected in oscillation mode. *Methods Enzymol* 276:307–326.
42. Terwilliger TC, Berendzen J (1999) Automated MAD and MIR structure solution. *Acta Crystallogr D Biol Crystallogr* 55(Pt 4):849–861.
43. Terwilliger TC (2000) Maximum-likelihood density modification. *Acta Crystallogr D Biol Crystallogr* 56(Pt 8):965–972.
44. Cowtan K (2006) The Buccaneer software for automated model building. 1. Tracing protein chains. *Acta Crystallogr D Biol Crystallogr* 62(Pt 9):1002–1011.
45. Murshudov GN, Vagin AA, Dodson EJ (1997) Refinement of macromolecular structures by the maximum-likelihood method. *Acta Crystallogr D Biol Crystallogr* 53(Pt 3):240–255.
46. McCoy AJ, Grosse-Kunstleve RW, Storoni LC, Read RJ (2005) Likelihood-enhanced fast translation functions. *Acta Crystallogr D Biol Crystallogr* 61(Pt 4):458–464.
47. Emsley P, Cowtan K (2004) Coot: model-building tools for molecular graphics. *Acta Crystallogr D Biol Crystallogr* 60(Pt 12 Pt 1):2126–2132.

SI Materials and Methods

Synthesis of 5-chloro-3-[(2E,6E)-8-hydroxy-3,7-dimethylnona-2,6-dienyl]-2,4-dihydroxy-6-methyl-benzaldehyde. (E,E)-2,6-Dimethyl-8-(tetrahydropyran-2-yloxy)octa-2,6-dienal (1) was reacted with MeLi (2 eq) in THF at −85 °C to give (E,E)-3,7-dimethyl-9-(tetrahydropyran-2-yloxy)nona-3,7-dien-2-ol. The secondary alcohol was acetylated with acetic anhydride (2.5 eq) in chloroform in the presence of Et_3N (3.0 eq), and DMAP (0.1 eq) at 25 °C (two steps, 93% yield). The acetate was treated with pyridinium p-toluenesulfonate (0.4 eq) in methanol at 55 °C to give (E,E)-8-hydroxy-1,2,6-trimethylocta-2,6-dienyl acetate (96% yield). The primary alcohol was brominated with CBr_4 (3 eq) and $(n-C_8H_{17})_3P$ (3 eq) in ether at 0 °C. Coupling of the bromide with 3-chloro-4,6-dihydroxy-2-methylbenzaldehede was performed by using a modification of the previously reported method (2) to produce (E,E)-8-(3-chloro-5-formyl-2,6-dihydroxy-4-methyl)phenyl-1,2,6-trimethylocta-2,6-dienyl acetate (two steps, 22% yield). After hydrolysis of acetate with K_2CO_3 (4.5 eq) in methanol at 25 °C, the final product was purified by silica gel column chromatography (hexane/AcOEt, 5:1, 70% yield). ^{1}H NMR (CDCl$_3$, 400 MHz)   1.20 (d, J=6.2 Hz, 3H, CH(OH)CH$_3$), 1.48 (br s, 1H, OH), 1.59 (s, 3H, CH$_3$), 1.78 (s, 3H, CH$_3$), 2.03-2.07 (m, 2H, CH$_2$), 2.08-2.16 (m, 2H, CH$_2$), 2.60 (s, 3H, Ar-CH$_3$), 3.40 (d, J=7.0 Hz, 2H, Ar-CH$_2$), 4.17 (q, J=6.2 Hz, 1H, CHOH), 5.21 (t, J=7.0 Hz, 1H, CH=C), 5.32 (t, J=6.6 Hz, 1H, CH=C), 6.61 (s, 1H, Ar-OH), 10.14 (s, 1H, CHO), 12.71 (s, 1H, Ar-OH). IR (KBr) 3200-3500, 1616 cm^{-1}.

Crystallization. The oxidized form of alternative oxidase from *Trypanosoma brucei brucei* was expressed, purified and crystallized as previously described (3, 4). We

modified the crystallization condition and obtained crystals suitable for X-ray analysis using the hanging-drop vapor-diffusion method at 20 °C. A 1 µl droplet of 3-5 mg ml^{-1} protein solution in 20 mM Tris–HCl pH 7.3, containing 0.8% (w/v) n-octyl -D-glucopyranoside (OG), 0.4% (w/v) tetraethylene glycol monooctylether (C$_8$E$_4$), 20 mM MgSO$_4$, 1 mM ammonium Iron (II) sulfate and 20% (v/v) glycerol was mixed with the same amount of reservoir solution and equilibrated against 200 µl reservoir solution (28–34% (w/v) PEG 400, 100 mM imidazole buffer pH 7.4, 500 mM potassium formate) to give crystals of TAO.

Data collection and phasing. The crystal of TAO soaked briefly in the cryo-protectant solution (50 % (w/v) PEG 400, 100 mM imidazole buffer pH 7.4, 500 mM potassium formate, 0.8 % OG, 0.4% (w/v) C$_8$E$_4$) was flash-frozen in liquid nitrogen. For phasing by SAD method, anomalous scattering effects caused by Fe were measured to 3.2 Å resolution using an X-ray with wavelength of 1.7390 Å at KEK-PF beamline BL17A (Tsukuba, Japan). The data set was processed and scaled with HKL2000 (5). SOLVE program (6) was used to locate and refine four "diiron sites" (FOM=0.195). RESOLVE (7) was used for solvent flattening assuming 62% solvent content (FOM=0.645). The map was clear to trace the TAO molecules. Initial model was built using RESOLVE (7) and BUCANER (8). Detailed analysis of the diffraction data shows that the crystal of Fe-SAD data was pseudo-hemihedral twinning and belong to space group C2 with unit cell parameters a = 148.4, b = 223.0, c = 62.7 Å and = 114.9°, and four monomers in the asymmetric unit. Amplitude-based twin-refinement using REFMAC5 (9) decreased R$_{work}$/R$_{free}$ drastically from 0.307/0.363 to 0.250/0.310. X-ray diffraction data of ligand-free TAO crystal was collected to 2.85 Å resolution at 100 K at SPring-8 beamline BL41XU (Harima, Japan). The crystals of the TAO-inhibitor complex were prepared by

2

soaking TAO crystals in the cryo-protectant solution supplemented with 1 mM AF2779OH for 150 min and 1 mM CCB for 90 min at 20 °C. The data were collected to 2.6 and 2.3 Å resolution for TAO-AF2779OH and TAO-CCB, respectively at 100 K at BL44XU (SPring-8). All data sets were processed and scaled with HKL2000 (5).

Refinement. The initial model of inhibitor-free TAO was determined by molecular replacement (MR) using the model obtained by SAD (3.2 Å resolution) as a search model. The program, Phaser (10) in CCP4i was used for MR. The models of the TAO-AF derivative complexes were successively obtained by MR using the refined structure of TAO. The models of ligand-free TAO and TAO-AF2779OH complex were re-built with reference to the well refined model of TAO-CCB complex at 2.3 Å resolution. Manual re-building and crystallographic refinement of all structures were performed using the COOT (11) and REFMAC5 (9). All structures were refined by amplitude-based twin-refinement in REFMAC5 (9) to final R_{work}/R_{free} values of 0.192/0.247 (twin fraction of 0.476), 0.214/0.256 (twin fraction of 0.552) and 0.185/0.227 (twin fraction of 0.527) for ligand-free TAO, TAO-AF2779OH, TAO-CCB, respectively. Stereochemistry of the refined structures, validated by PROCHECK (12) and Ramachandran plots indicated that no amino acid residues were detected in energetically unfavorable regions. Out of 329 amino acid residues constituting the whole TAO protein, chains A, B, C and D in the asymmetric unit are comprised of residues: 31-297, 32-299, 32-297 and 32-297, respectively for the ligand-free; 30-295, 32-296, 31-296 and 30-295, respectively for the TAO-AF2779OH complex; and 32-295, 31-296, 32-297 and 32-294, respectively for TAO-CCB complex. Data collection and structural refinement statistics are summarized in Table S1. Figures showing protein structures were prepared with the graphics program PyMol (http://www.pymol.org/).

3
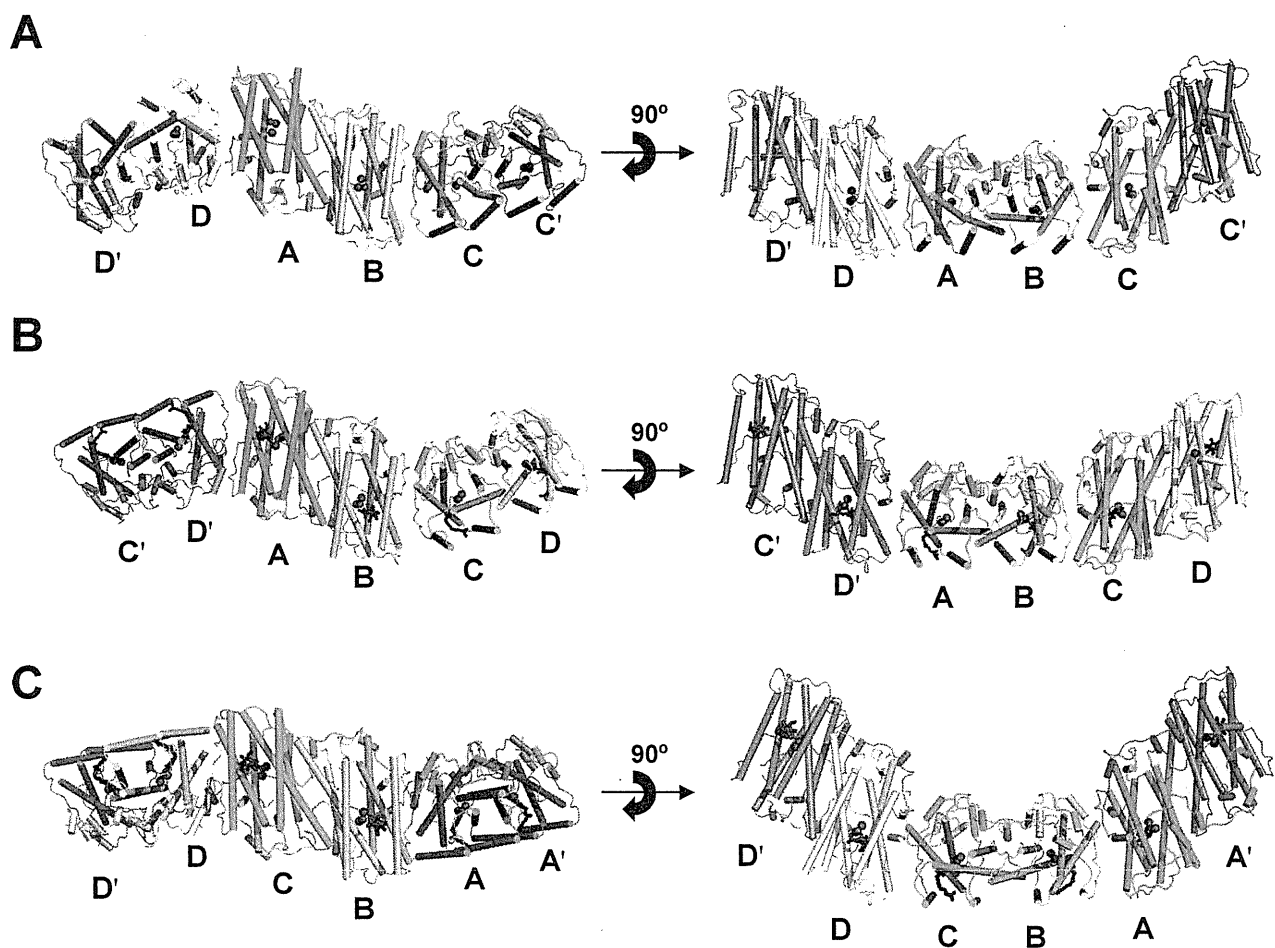
Fig. S1. Crystal packing of TAO molecule. Crystal packing of chains A, B, C and D in the asymmetric units of (**A**) AF2779OH-free TAO, (**B**) TAO-AF2779OH and (**C**) TAO-CCB complex viewed from two directions perpendicular to each other. Chains A, B, C and D are colored in light green, light pink, cyan and yellow. Diiron and hydroxo atoms are shown as the magenta spheres and the bound AF2779OH or CCB as red stick. In (**A**) and (**B**), chains C' and D' are related to chains C and D, respectively, by crystallographic 2-fold axes. A-B, C-C' and D-D' pairs form dimers in **A**, whereas A-B, C-D and C'-D' pairs in **B**. Chains C' and D' are colored in dark blue and orange, respectively. In (**C**), chains A' and D' are related to chains A and D, respectively, by crystallographic 2-fold axes. A-A', D-D' and B-C pairs form dimers in **C**.

4
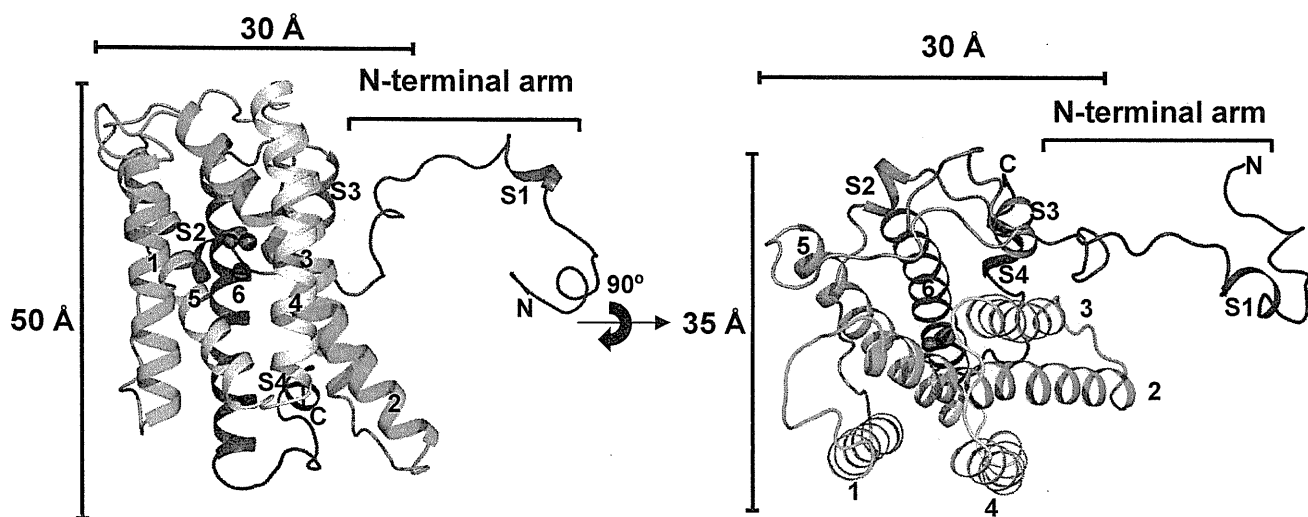
Fig. S2. Monomer structure of TAO. Ribbon representation of chain A viewed as in Fig. **1A**. Monomer structure of TAO viewed roughly perpendicular (left) and parallel (right) to the helix axes. Chain A is colored in rainbow from blue (N-terminus) to red (C-terminus). Except for the N-terminal arm, each monomer is shaped as a compact cylinder ($50 \times 30 \times 35$ Å). The diiron (Fe-OH$^-$-Fe) is drawn as magenta spheres.
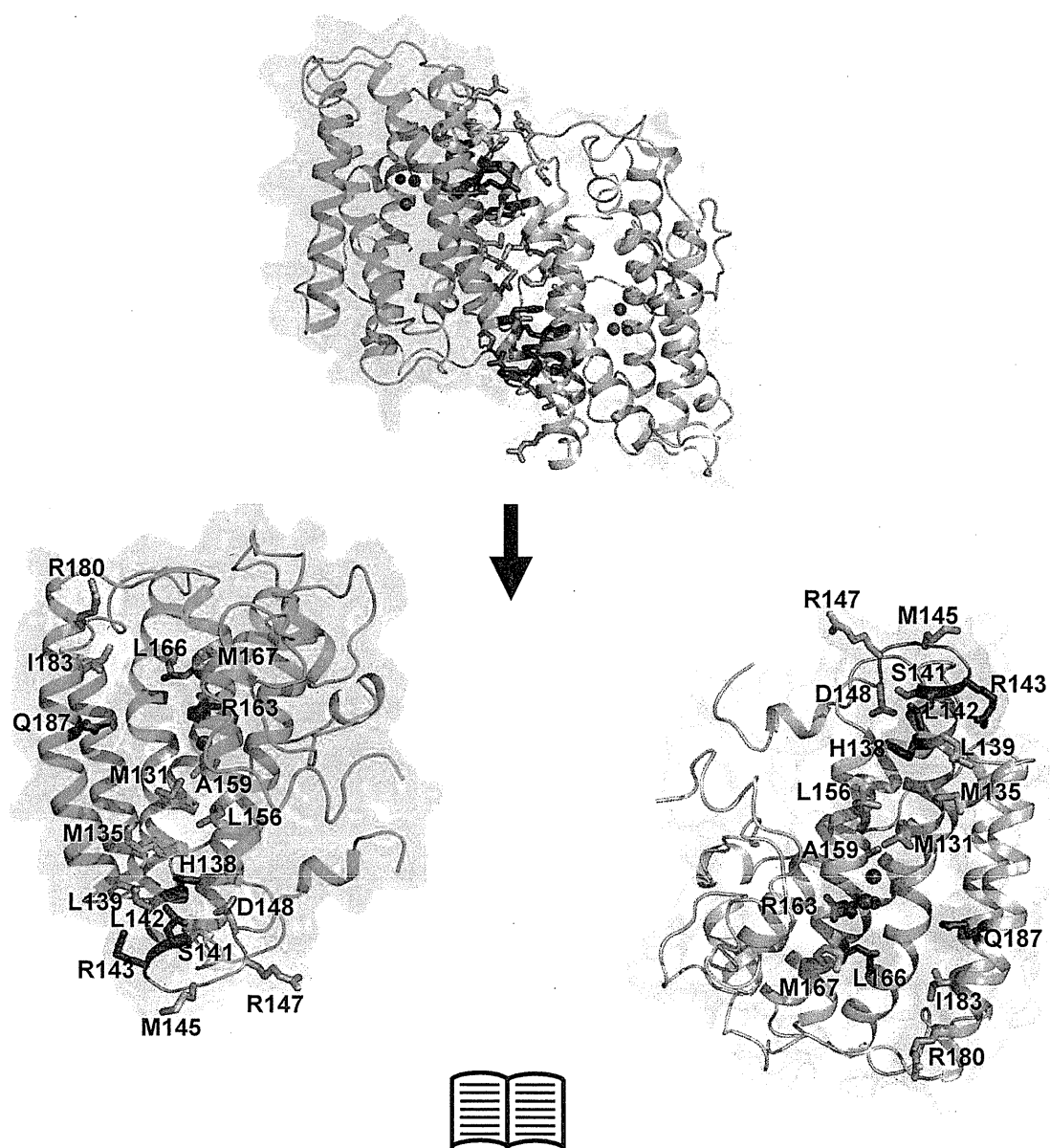
Fig. S3. Dimer interface of the TAO dimer. The upper panel represents the TAO dimer formed by the A-B pair of the AF2779OH-free TAO viewed from the same direction as Fig. **1A** (left panel), and the lower is the 'open book' representation of the upper. Chains A and B are colored in light green and light pink, respectively. Residues conserved in all eight and more than four species (Fig. **S5**) are colored in red and orange, respectively.

Fig. S4. The proposed membrane binding model of the TAO dimer viewed from four directions. The colour codes are as in Fig. **1C**. Conserved basic residues located on the interface between TAO and the membrane are colored in blue. Residues name are labeled black (asterisks denotes in chain B).

7

```
                1                    20            40              60
                ················································  S1
T.brucei          --------------------MFRN-------------------HASRITAAAAPWVLRTACRQKSDAKTPVWGHTQLNRLSFLETVPVVPLRVSDESSEDRP---------------
C.parvum          ---------------------MYYVRNLSHTNKLRYFYGRHLWLLSSKVNLNNLCSIVHSNKGQKITSKLYIITLEKDRSSNNQGGFSKKRTLECKSDQINKFDAENEEKVGSHFMKKSN
S.guttatum        -------------------MISSRLAGTALCRQLSHVPVPQYLPALRPTADTASSLLHRCSAAAPAQRAGLWPPSWFSPPRHASTLSARAQDGGKEKAAGTAGKVPPGEDGGAEKEAV
C.reinhardtii     MLQTAPMLPGLGPHLVPQLGALASASRLLGSIASVPPQHGGAGFQAVRGFATGAVSTPAASSPGHKPAATHAPPTRLDLKPGAGSFAAGAVAPHPGINPARMAADSASAAAGASGDAALA
N.aromaticivorans --------------------------------------------------------------------------------------------------------------------
N.crassa          ----------------------------------------MNTPKVNILHAPGQAAQLSRALISTCHTRPLLLAGSRVATSLHPTQTNLSSPSPRNFSTTSVTRLKDFFPAKET
C.albicans        -------MIGLSTYKKVPTLLATTTITTVTSTTLRSNQLLRLASTTSTKPNASTTVAAAAAAATNSLGNSNSKLPIDKNDLEKPGTIPGKHKPFNIQTEIYNQAGIEANDDDKFLTNPT
C.intestinalis    MLSTGSKTFLFRPFLGSCHALQSGKLPCSNLHTTPTKITVKRYLVGYSWSTQPHSRLLHSCQQLKIDDKNKSEHFKIETNDSTDEPNIEVENFPHFREAKKAKETQKGSSLAEAEEHPDV
```

```
        S2                80          100               120         2
                                                         ++  +                ++ +++        140
T.brucei          --TWSLPD-----------------------IEN...KKENGLVD...YRS...RTC.....TSL...CS---------------I..SKVIS...FLETVAGVPGMVGGMLRHES
C.parvum          HAASILEGKEYG------------FNSPIWDLEEVNN...LC..GFKD..SYYI...KS..LLTR..K.---------------HN.....CRR.FLETVAGVPGMVGA.MLRH.FS
S.guttatum        VSYWAVPPSKVSKEDGSEWRWTCFRPWETYQADLSIDLHN...HV...IL...LR..KA..W.....L..QR..A-----------CRA......TVA.VPGMVGGV.LH.K
C.reinhardtii     ESYMAHPAYS-----------------DEYVES...P..VT..QKLHQHVGLRTIQVF....L..KA..Y..PTG---------------SM..A..RR.MS.EBVVAGC.CMVA.GMLRH.K
N.aromaticivorans ----MIPP--------------------FIDLSV.HK.GGLS.RI..FGFTKA..CA...FAE.C---------------H.AVV..V.AVPG.VGATIN..A
N.crassa          AYIRQTPPAWPHHG-------------WTEEEMTS..VP..RK.ETVGD...WKL..RICR..AI.IATC..PEQQVDKHHPTTATSADKPL..A...VRF.IFLES.AGVPGEMVA.GMLRH.R
C.albicans        YRHEDFTEAG-----------------VYR..HV..R..RTTGD..ISCYGTLFF..KC..LVT.G.AVPDPDKPDQYKG---TRWEM.SGK.T.CIFLES.AGVPGG.VA.GFVRH.H
C.intestinalis    EEGRAMQDGGYRLPHP-----------IWHKQELES.RIS..RP.VGKVD...YS..QL.T..G.D.RSC.TLC.YTGRLD----------G.K.VKR.IFLE.I.AGVPGMVG..VEBH.V
```
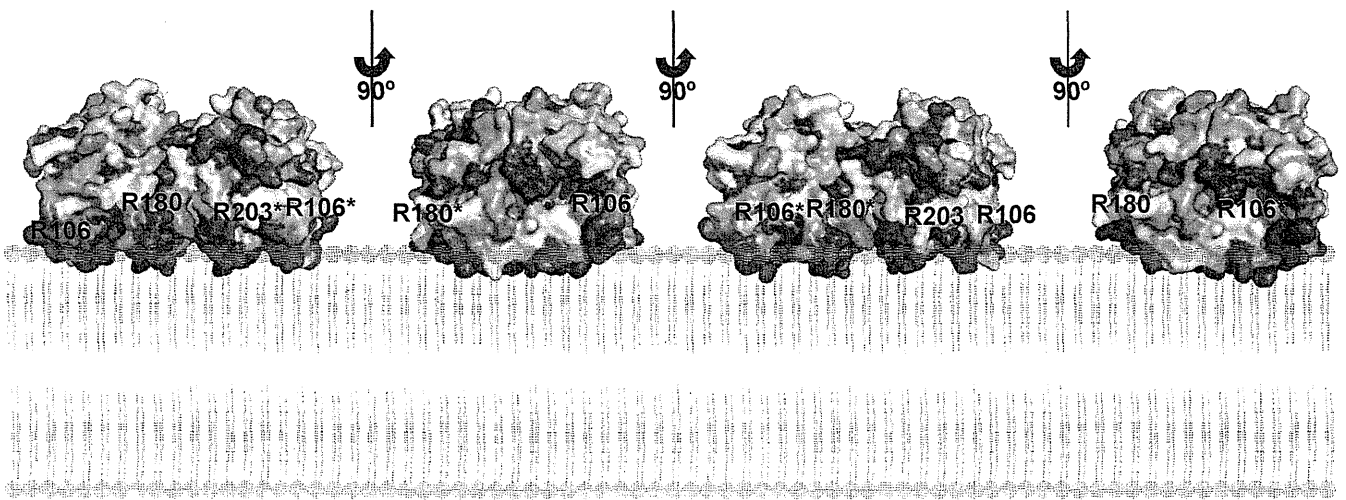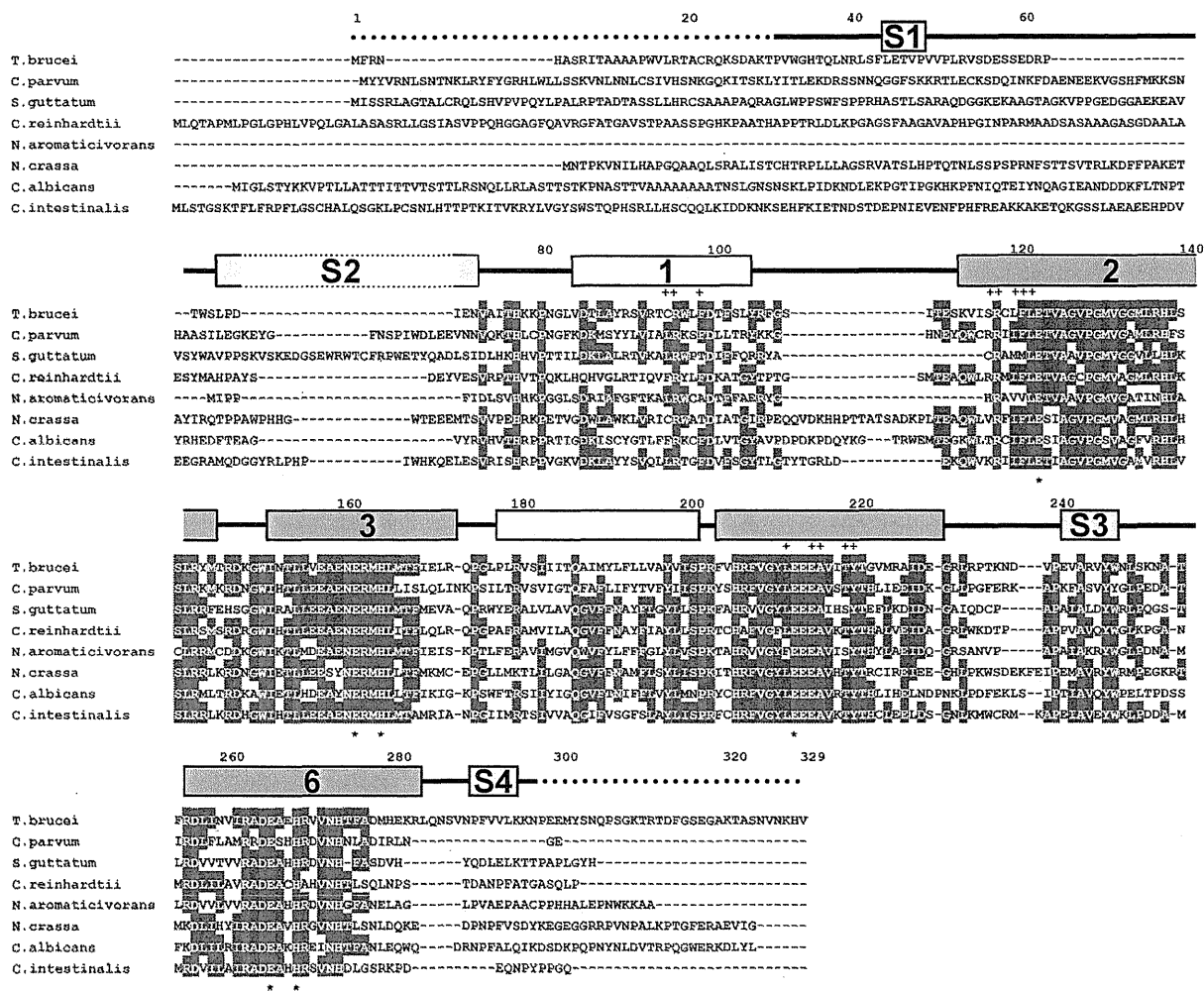
```
              160         180          200            220         S3
                                                     +  ++  ++           240
T.brucei          SIR..MTRDK..TIN.TL...A.AENER.MHIL..TELR-Q..LPL.VS..IIT..AIMYLFLLVA..V..P.RFV..REVGY.EEE.AV...GVMRA..E-GR..RPTKND---V..EV..RV...SKN...
C.parvum          .IR..K..N.TL..H..EEA.ENER.MHIL.ISLQLINK..SILT.VSVIGT..FA.LIFYTVP...L..RYS.REVGY.EEE.AVS...LIP..DK-Q.LPPGFERK----...KF..SV..G..EDA...
S.guttatum        .IR.FEHSCG..IRA..EA.ENER.MHIL..F.MEVA-Q.RWYP.RALVLAV.GVF..AY.G.YL.SD.FAH.VVG.YLEEE.IHS.TEF.KD...N--GAIQDCP-----..A..L.DA.R.QGS--..
C.reinhardtii     .IR.A...D.GT.H.L..EEA.ENER.MHIL..F.LQLR-Q..PA.AMVILA.GVF..AY.IA.GFL.S.RTC.A.VG.FLEEE.AV...KM.U.AV.VA...F.WKDTP----...PVA.Q.A.G.PKPG--N
N.aromaticivorans C.RR..CD.K.C..TK..TMDEA.ENER.MHIL..F.EIS-K.TLFF.AV.MGV.V.TYLFF.GL.T.VS.PK.TAH..VVG.EEE.AVIS.T.M.A..TIQ-GRSANVP-----...AL...L.KR..G..DNA-M
N.crassa          .IR..LK.DN.T.E..T..ESY.NER.MHIL..HKMC-E..GLLMKTL.LGA.GVF..AM..TS.L.R.KITH.REVG.EEE.AV..A.CRIR..EE-C..PKWSDEKFEI..EMA.R.T.RM..EGKR..
C.albicans        .IR..MLT..D.KA..TE.T.HDEA.ENER.MHIL..TKIG-K..SWF.T.SI.YIG.GVF..IF..V...MN.P.YCHRFVGY.EEE.AVR.T.LIH..LNDPNK.PPDFEKLS--I...AV..Q..PELTPDSS
C.intestinalis    .IR..LK..D.CW.T.H..EA.ENER.MHIL..AMRIA-N..IIM.T.VVA.G.L.VSGFS.A...IS.RFC.RE.VG.EEE.AV.....C.P..DS-G.N.KMWCRM--.A...E...K..DD..-M
```

```
              260         280      S4
                                                   6
T.brucei          FRDL.NV.RADEA..HR.VN.T.A.DMHEKRLQNSVNPFVVLKKNPEEMYSNQPSGKTRTDFGSEGAKTASNVNKHV
C.parvum          IRDF.LAM.R.DES.HR.VN.NL.DIRLN---------------GE----------------------
S.guttatum        LRD.VVTVV.RADEA..HR.VNH-.A.SDVH-------YQDLELKTTPAPLGYH---------------------
C.reinhardtii     MRDL..AV.RADEA.C.AH.VNH.LSQLNPS--------TDANPFATGASQLP---------------------
N.aromaticivorans L.D.VV.VV.RADEA..HR.VNH.G.F.NELAG------LPVAEPAACPPHHALEPNWKKAA----------------
N.crassa          MKD.L.HY.RADEA.V.HR.GVNH.LSNLDQKE-----DPNPFVSDYKEGEGGRRPVNPALKPTGFERAEVIG------
C.albicans        FKD.I.R.R.RADEA.K.HR.IN.T.A.NLEQWQ----DRNPFALQIKDSDKPQPNYNLDVTRPQGWERKDLYL------
C.intestinalis    M.D.V.T.A.RADEA..HR.VNH.DLGSRKPD----------EQNPYPPGQ--------------------
```

Fig. S5. Multiple alignment of amino acid sequences of alternative oxidases. The alignment was produced from amino acid sequences from Trypanosoma brucei brucei (protozoa), Cryptosporidium parvum (protozoa), Sauromatum guttatum (plant), Chlamydomonas reinhardtii (alga), Novosphingobium aromaticivorans (α-proteobacteria), Neurospora crassa (mold), Candida albicans (anascosporogenous yeast) and Ciona intestinalis (chordata). The secondary structure elements identified in the TAO structure are also shown. Helices α1 and α4, which form the hydrophobic region on the molecular surface of TAO and are proposed to be concerned in membrane binding, are colored in yellow. Helices α2, α3, α5 and α6, which form the four helix bundle to accommodate the diiron centre, are colored in cyan. Amino acid residues coordinating the diiron centre and interacting with AF2779OH are indicated by * and +, respectively. Cyan and pink colours stand for conservation of AOX residues in all 8, and over 4 organisms, respectively.
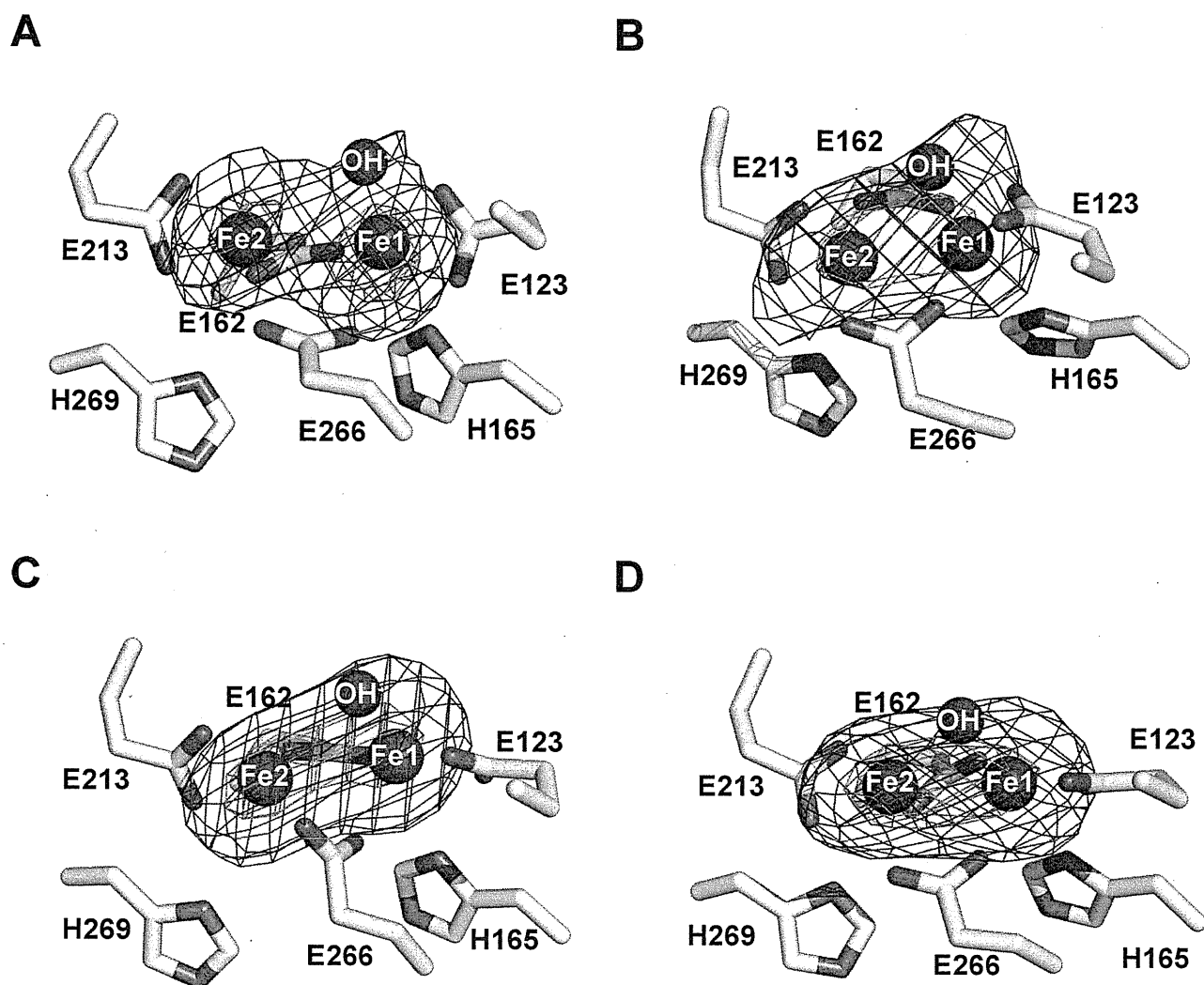
8

Fig. S6. The structure of diiron sites. Interaction between the diiron molecule and TAO with sigma-A weighted electron density map (Fo-Fc) calculated from the refined model of ligand-free TAO with the diiron molecule omitted from the phase calculation. The diiron molecules bound to (**A**) chain A, (**B**) chain B, (**C**) chain C and (**D**) chain D are shown as yellow sticks with nitrogen and oxygen atoms colored in blue and red. The diiron (Fe-OH⁻-Fe) is drawn as magenta spheres. Contour levels are 1.0 (blue) and 3.0 (orange).

9
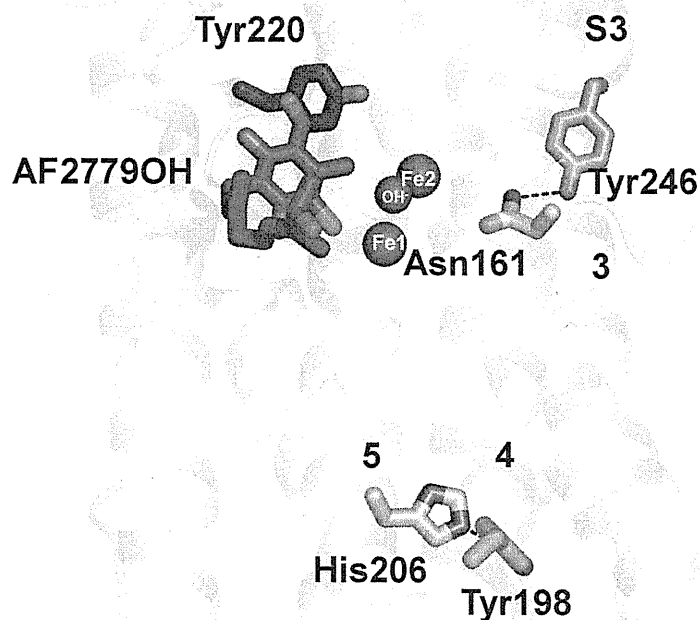
**Fig. S7. Conserved tyrosine residues.** The bound AF2779OH molecule is shown as red stick. Tyr220

(blue) is located near the diiron and AF2779OH, but Tyr198 and Tyr246 (orange) are far from both the diiron

(magenta spheres) and AF2779OH. The interacting residues of these tyrosines are shown as light pink stick

models and dash lines stand for hydrogen bonds.

10
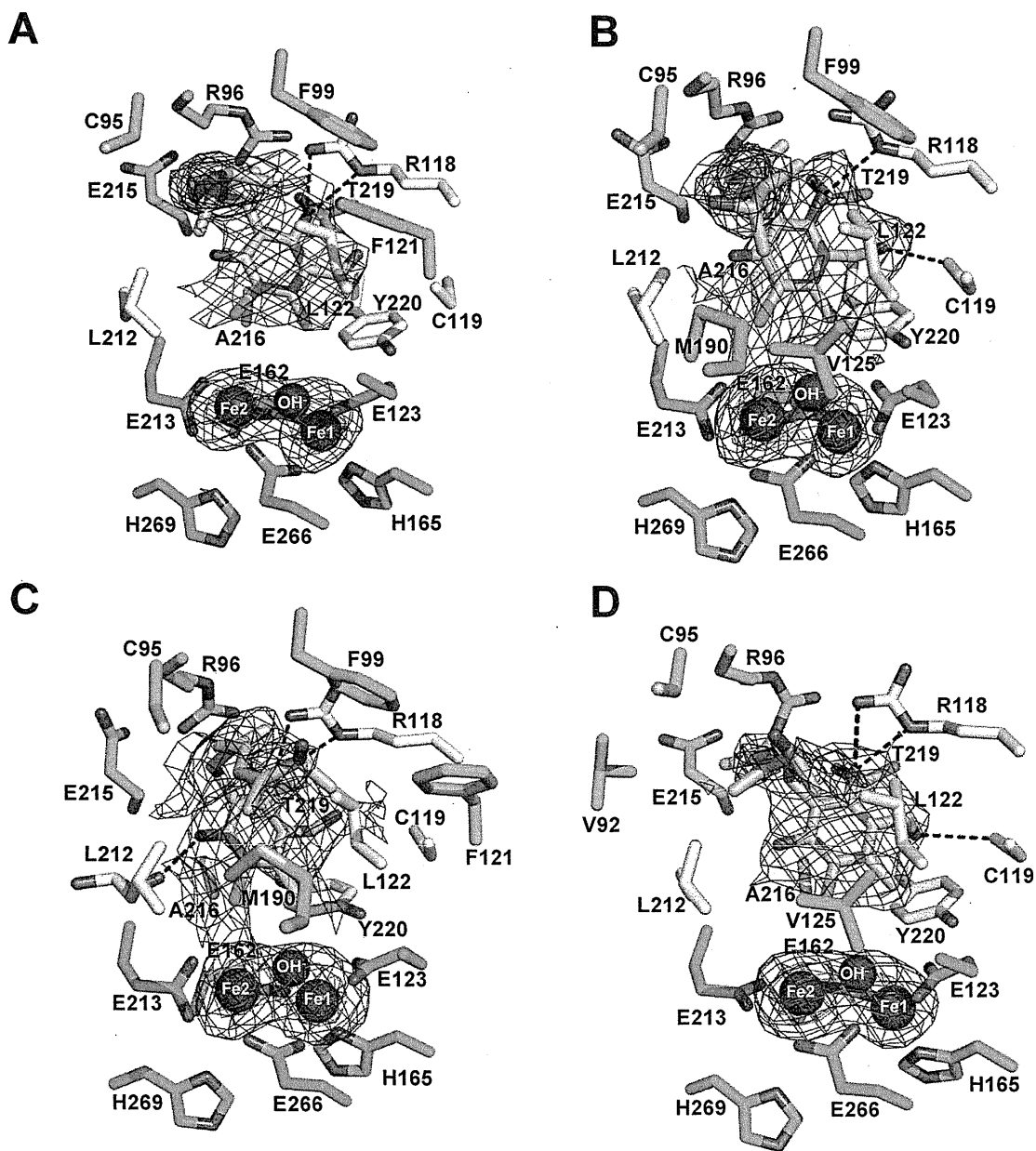
Fig. S8. Interaction between TAO and the bound AF2779OH molecules and their electron density maps. Interaction between the bound AF2779OH molecule and TAO with sigma-A weighted electron density map (Fo-Fc) calculated from the refined model of TAO-AF2779OH complex with the AF2779OH molecule omitted from the phase calculation. AF2779OH molecules bound to (**A**) chain A, (**B**) chain B, (**C**) chain C and (**D**) chain D are shown as pink sticks with nitrogen, oxygen and chlorine atoms colored in blue, red and green, respectively. The diiron (Fe-OH⁻-Fe) is drawn as magenta spheres. Contour levels are 1.0 (blue) and 3.0 (orange).

11
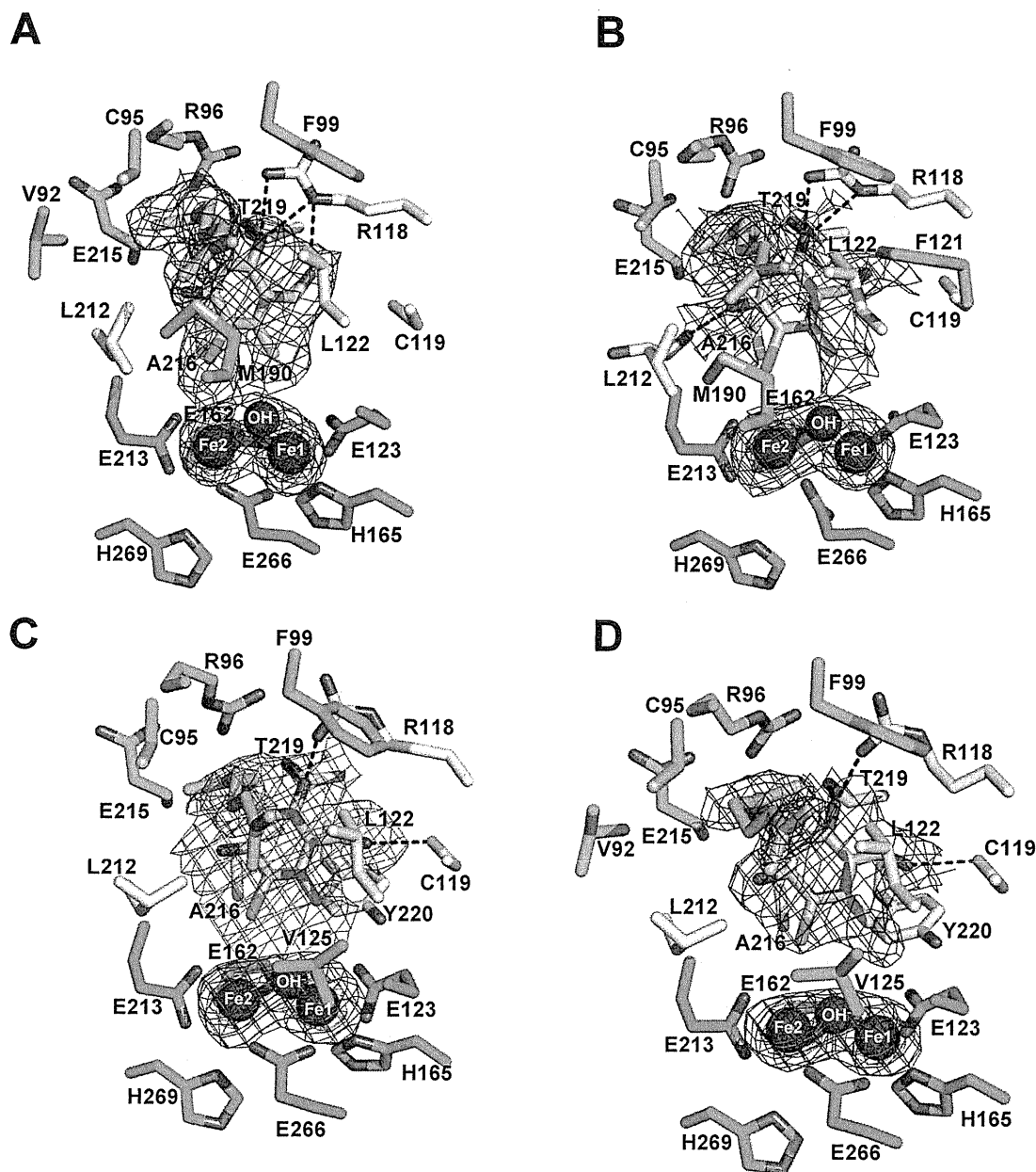
Fig. S9. Interaction between TAO and the bound CCB molecules and their electron density maps.
Interaction between the bound CCB molecule and TAO with sigma-A weighted electron density map (Fo-Fc) calculated from the refined model of TAO-CCB complex with the CCB molecule omitted from the phase calculation. CCB molecules bound to (**A**) chain A, (**B**) chain B, (**C**) chain C and (**D**) chain D are shown as pink sticks with nitrogen, oxygen and chlorine atoms colored in blue, red and green, respectively. The diiron (Fe-OH⁻-Fe) is drawn as magenta spheres. Contour levels are 1.0 (blue) and 3.0 (orange).
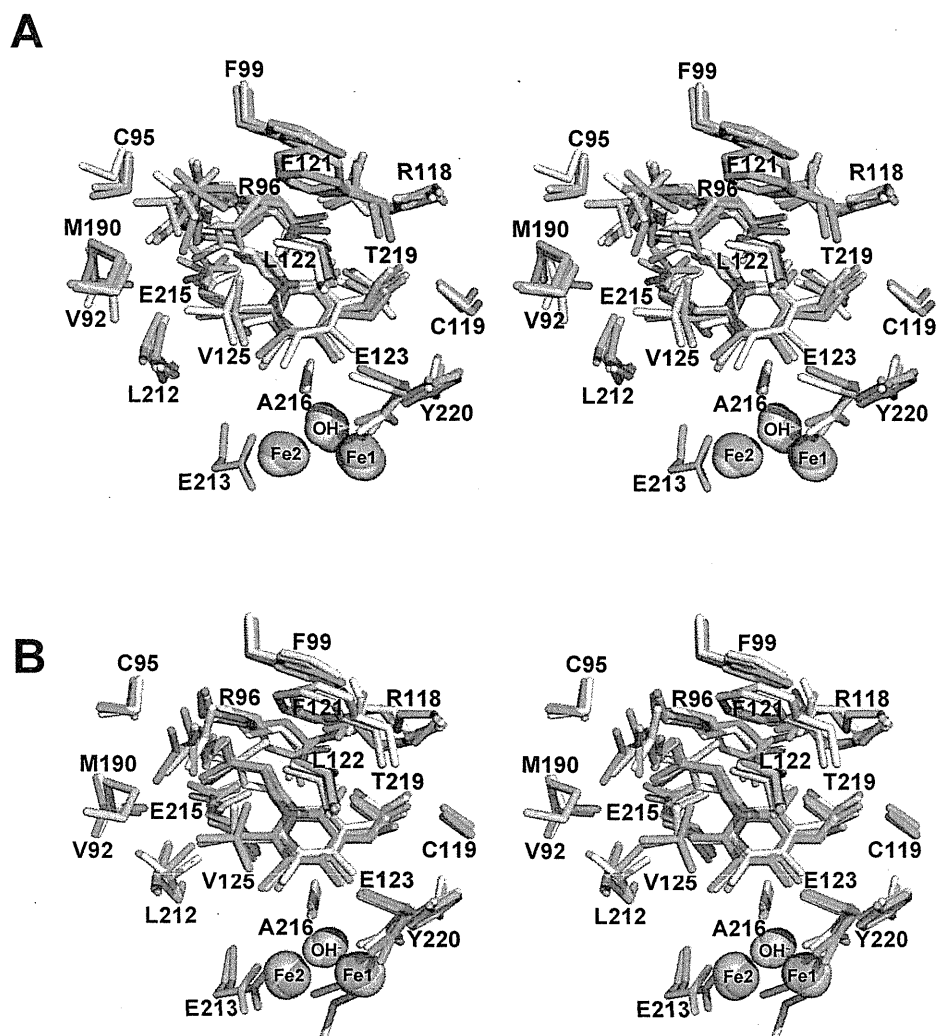
Fig. S10. Stereo view of superposed inhibitor binding site of all chains of the complex structures. (A) AF2779OH-TAO and (B) CCB-TAO. Chains A, B, C and D are colored in light-green, light-pink, cyan and yellow, respectively.
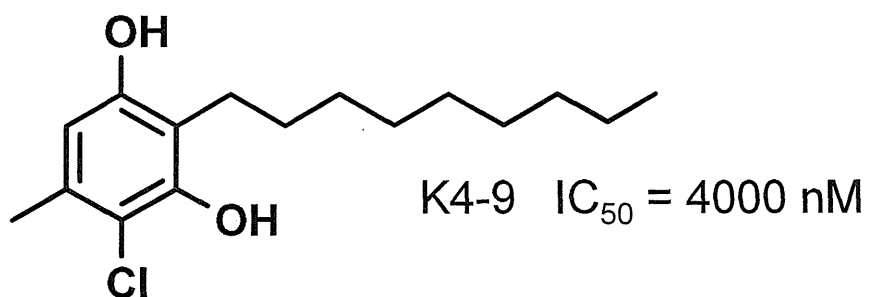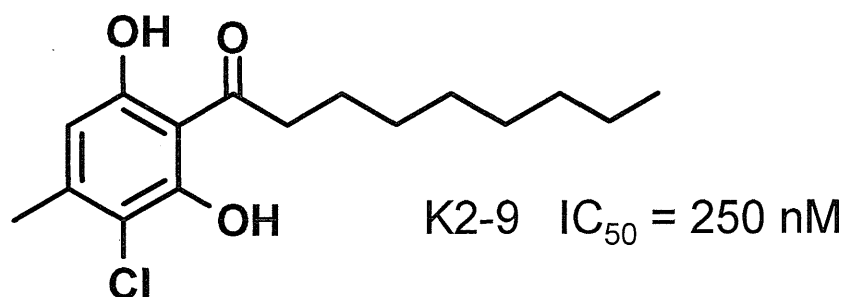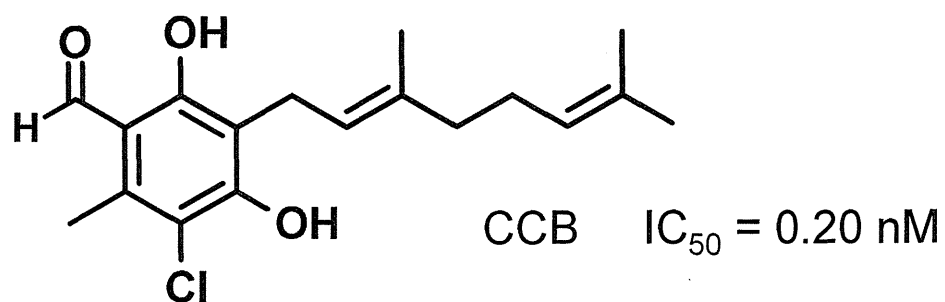
AF2779OH $IC_{50} = 0.48$ nM

CCB $IC_{50} = 0.20$ nM

K2-9 $IC_{50} = 250$ nM

K4-9 $IC_{50} = 4000$ nM

Fig. S11. IC_{50} of the AF derivatives. IC_{50}s of the AF derivatives with (AF2779OH and CCB) and without (K2-9 and K4-9) the aldehyde group.
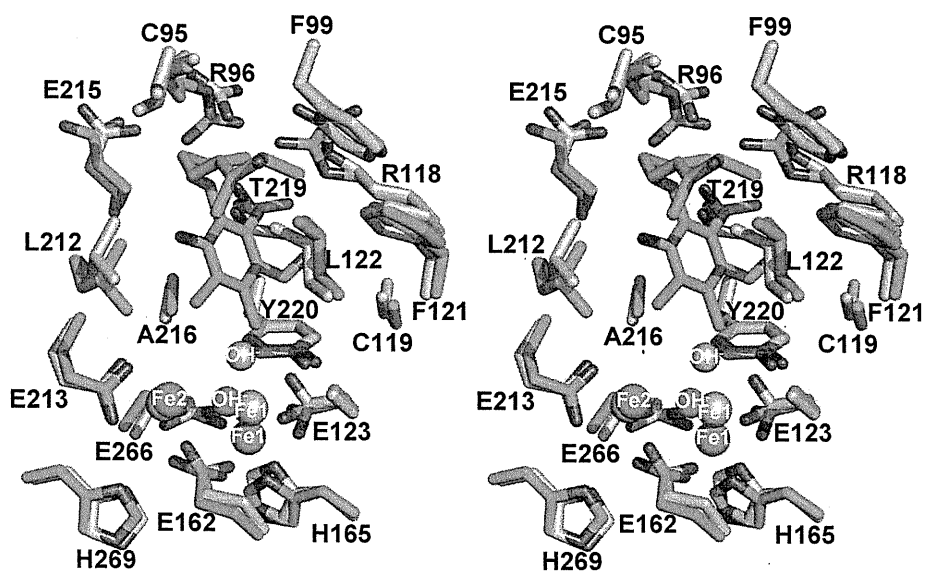
14

Fig. S12. Stereo view of inhibitor-free TAO and AF2779OH-TAO complex around active site. Inhibitor-free TAO and AF-2779OH-TAO complex are shown in light-pink and light-green sticks, respectively. Unlike amino acid residues, the diirons poorly superimposed on each other.
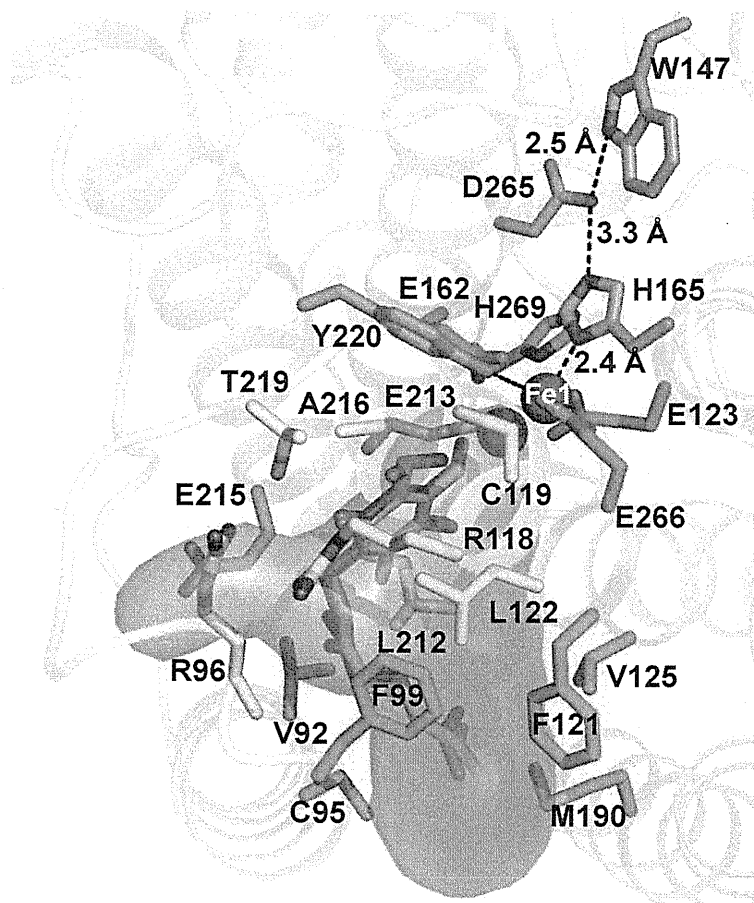
Fig. S13. Putative ubiquinol binding channels in CCB-TAO complex. Two hydrophobic cavities found by CAVER protein-analysis software (13) are shown by green and orange. Proposed residues involved in electron transfer are shown as orange sticks.